

# Aerodynamic and Aeroacoustic Analysis of Looped Propeller Blades

Justin du Plessis\* and Abdesslem Bouferrouk†  
*University of the West of England, Bristol, BS16 1QY*

**This paper investigates the potential of looped propeller blades to reduce aerodynamic noise through the diminution of blade vortex interactions. Flow simulations were conducted in ANSYS Fluent using high-fidelity LES combined with the Ffowcs William-Hawkings model to evaluate the acoustics of looped propeller blades. Experimental wind tunnel testing was conducted in static and forward flight conditions to validate the simulations and to assess the performance of the propeller blades. The comparison between numerical and experimental results shows good agreement for the thrust trends and noise spectra. Two design variations were tested to investigate the effect of changing the plane in which the looping occurs. Results show that the in-plane looped propellers have the capability to reduce noise generation by up to 10dB (OSPL) albeit with a reduction in both thrust performance and operational efficiency. Conversely, when loop occurs out of plane, it was found to have a slight increase in noise generation along with a reduction in efficiency. Flow visualization showed that looped propeller design seems to reduce the strength of tip vortices in comparison with the conventional propeller. Findings from this study may have applications for UAVs operating in urban environments, particularly in the design of novel low-noise propellers.**

## Nomenclature

$A$	=	propeller disk area
$c$	=	propeller chord length
$C_P$	=	power coefficient
$C_{P0}$	=	rotor power coefficient
$C_T$	=	thrust coefficient
$C_{T0}$	=	rotor thrust coefficient
$CFD$	=	computational fluid dynamics
$FM$	=	figure of merit
$J$	=	advance ratio
$n$	=	rotations per second
$p$	=	pressure
$P$	=	power
$r$	=	local radius position
$R$	=	total radius
$SPL$	=	sound pressure level
$T$	=	thrust
$V$	=	freestream velocity
$\eta$	=	efficiency
$\rho$	=	density
$\Omega$	=	rotational speed

---

\*Student, BEng(Hons) Aerospace Engineering

†Senior Lecturer, Aerospace and Mechanical Engineering, Corresponding Author: Abdesslem.Bouferrouk@uwe.ac.uk

## I. Introduction

The rapid advancement in drone and Vertical Take-Off and Landing (VTOL) technologies has rekindled interest in propeller-driven aircraft. One of the main strengths of propellers and a reason for their re-emergence of research interest in them is their high propulsive efficiency [1] and low maintenance requirements, a particularly important aspect in electrically driven rotary and fixed wing UAVs, and VTOL aircraft. The continued development of these aircraft has highlighted a critical societal challenge that could hinder their commercial use due to stringent regulations: the need for mitigation against noise pollution, especially from propellers. UAV open propellers naturally cause high levels of noise because there is no shielding mechanism to attenuate the noise. As these innovative aircraft become increasingly prevalent, particularly in urban environments, the need to develop quieter propeller designs that minimize aerodynamic noise has become paramount.

Aerodynamic noise is generally split up into either tonal or broadband noise [2]. Propeller Noise is complex because of its many sources, some of which are still not well-understood. The tonal noise of a propeller is typically influenced by the propeller's blade passing frequency, its higher-order harmonics, laminar boundary-layer vortex shedding, propeller trailing-edge bluntness and blade vortex interactions (BVI). Broadband noise is typically influenced by factors such as the shape of the blades (e.g. twist and pitch distributions, chord length, diameter, trailing-edge thickness), trailing edge turbulent boundary layer, the blade wake interaction (BWI) and again the blade vortex interaction (BVI). The BVI one of the main noise sources impacting the usage of rotorcraft in urban environments [3]. Noise generated because of BVI is dependent on several factors including the vortex circulatory motion, the vortex core size and the turbulence levels present within the vortex [4]. More critically perhaps, the noise is altered through its interaction with the tip of the propeller, and as such is dependent on the geometrical shape of the propeller tip. Consequently BVI impacts both the tonal and broadband noise. For this reason, the current investigation focuses mainly on the effects of propeller tip vortices.

As the noise generated by a propeller is a result of small rapid pressure fluctuations, mainly within the boundary layer and much smaller than general aerodynamic pressure fluctuations, numerical predictions of noise generally involve using a method that decouples the pressure fluctuations from each other. The Ffowcs Williams-Hawkings (FW-H) acoustics model is typically integrated into the CFD simulations for this purpose, as it is able to decouple the sound generation and propagation from its source and environment, only relying on the pressure fluctuations on the surface of the propeller[5]. This makes it well suited to cases where far-field noise analysis is desired.

Several noise mitigation methods for propellers exist already - one such method is to decrease the speed at the tip of the propellers by using a larger propeller at lower RPMs, which reduces the intensity of the blade's passing frequency [6]. Another commonly implemented method is altering tip geometry in the form of anhedral tips, which can reduce the wake interactions of the blade tip as demonstrated by Hanson et al. [7].

This study addresses the challenge of noise reduction by introducing a novel design change in the form looped propellers, inspired by MIT's Toroidal Propeller concept [8], and the Sharrow Marine Propeller [9]. Furthermore, the current work is inspired by the findings of Treuren et al. [10] who showed that noise from standard quadcopter propellers can be reduced using leading-edge notches which disrupt the formation of propeller tip vortices. Focusing on both the aerodynamic and aeroacoustic performance, this paper aims to assess the ability of looped propeller designs in achieving quieter operation whilst maintaining a good operational efficiency. The research ultimately aims to answer the question; are looped propeller blades a viable solution to reduce the aerodynamic noise generated by UAV's? The research combines Large Eddy Simulations (LES) with FW-H in ANSYS Fluent to gain an initial understanding of potential noise reductions and to highlight any changes in performance brought about by such radical propeller designs. In parallel with flow simulations the looped propeller configurations were tested in UWE Bristol's anechoic chamber to simulate hovering flight using a setup inspired by Jordan et al[11], in addition to being tested in UWE Bristol's subsonic wind tunnel simulate forward flight. In both cases, apart from validating the simulations, the purpose was to understand changes in flight and acoustic performances, as well as observing changes in flow behaviour.

## II. Testing Methodology

### A. Propeller Designs

The propellers used for the research are based on the DJI 9450 and APC 10X5E. These propellers were selected due to their commercial availability and commonality amongst drone designs. The geometry of the DJI 9450 propeller blade was obtained from a freely available 3D scan of the propeller [12], whilst the APC 10X5E blade geometry was obtained using the data provided by APC propellers [13]. Figures 1 and 2 show the chord and twist distributions for the DJI 9450 and APC 10X5E, respectively. Table 1 lists further geometric and physical characteristics of the propellers.

**Table 1 Propeller Characteristics**

Propeller	Diameter, $m$	Disk Area, $m^2$	Manufactured Material	Mass, $kg$
DJI 9450	0.24	0.0452	PA-GF	0.008
APC 10X5E	0.254	0.0507	PA-GF	0.008

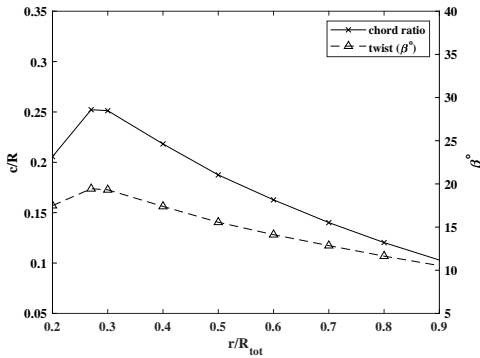


**Fig. 1 DJI 9450 Chord and Twist Distribution**

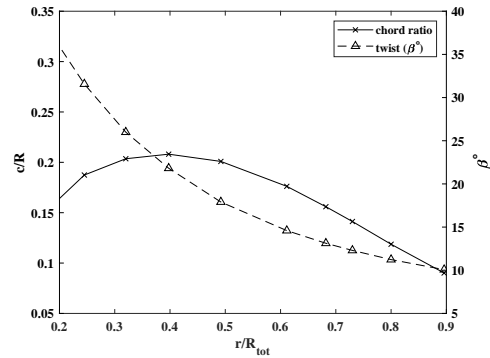


**Fig. 2 APC 10X5E Chord and Twist Distribution**

For a fair comparison between the looped propeller and a conventional design, several design constraints were introduced:

- Propeller diameter must remain constant.
- Chord lengths of the original propellers must be halved on each of the looped propeller's blades to maintain a similar surface area.
- The propellers must retain the same airfoils in the same span-wise locations.
- The airfoils must maintain the same twist along the blade.
- All propellers are manufactured using a Selective Laser Stinting process with Glass Filled Nylon [14]

Two sets of propellers were created using these constraints, each set features a standard propeller design as the reference propeller, a propeller with a loop in the horizontal axis ( $XZ$  Plane), labeled as Variant 1, and a second looped propeller with its loop in the vertical axis ( $YZ$  plane) labeled as Variant 2. Set 1 uses the DJI 9450 propeller as its reference design, and set 2 uses the APC 10X5E as its reference design. Figures 3 and 4 show the propeller sets.

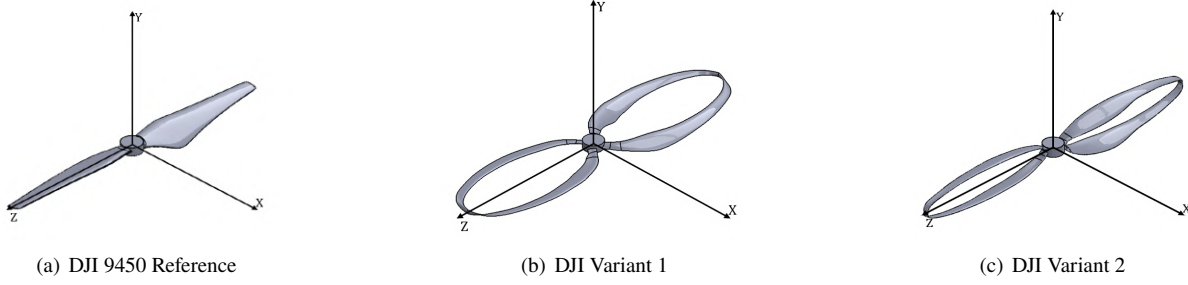


**Fig. 3 DJI 9450 Propeller Set**

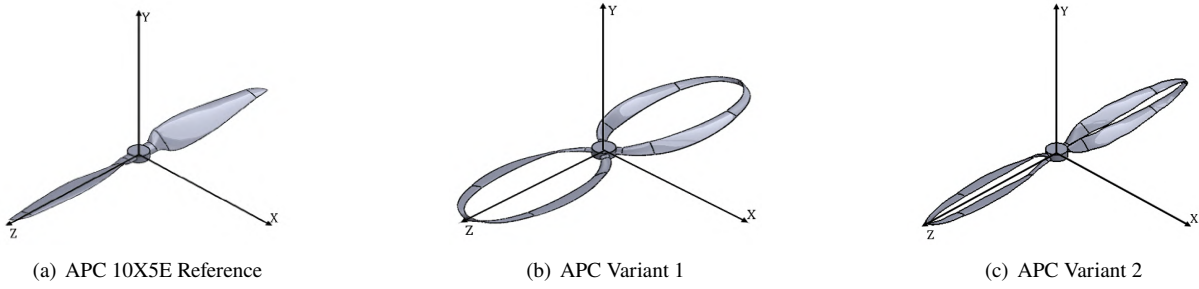


**Fig. 4 APC 10X5E Propeller Set**

For both propeller sets, Variant 1 is inspired by MIT’s toroidal propeller design [8] which investigated the effects of using the blades in a similar orientation. Research done by Shima et al. [15] showed that using the blades in this orientation has the potential to reduce noise but at a cost to the peak thrust and efficiency. Variant 2 is inspired by the design of annular wings and box wing designs, for which previous research has shown that such wings increase the lift-to-drag ratio of wings, through the attenuation of tip vortices [16],[17]. For this reason, they were evaluated as the second option to investigate the effects of a similar orientation when used in looped propellers.

## B. Propeller Performance Calculation

The performance of a propeller is commonly evaluated as a combination of its thrust and efficiency performance in both hover (static) and forward flight (non-static). As the performance of a propeller varies largely depending on the relative motion of the propeller, it is important to test it in both conditions to gain a more comprehensive understanding of its performance. The atmospheric pressure and temperature was recorded at the time of the experiments, and density was calculated using the equation of state, where  $R = 287 \text{ J/KgK}$ .

Equation 1 was used to calculate the thrust coefficient and equation 2 for the Power Coefficient ( $C_P$ ).

$$C_T = \frac{T}{\rho n^2 D^4} \quad (1)$$

$$C_P = \frac{P}{\rho n^3 D^5} \quad (2)$$

For measurements done in non-static conditions, with the wind tunnel providing freestream velocities ( $V$ ), the introduction of  $V$  allows for the calculation of advance ratio and efficiency which are calculated using equations 3-4 [18],[19].

$$J = \frac{V}{nD} \quad (3)$$

$$\eta = \frac{TV}{P} \quad (4)$$

To evaluate a propeller’s suitability to hover, a figure of merit ( $FM$ ) was calculated. The  $FM$  is the ratio of ideal power to hover and the required power to hover. Calculating the  $FM$  requires the recalculation of the  $C_T$  and  $C_P$  but viewing the propeller as a rotor instead,[7], hence gaining  $C_{T0}$  and  $C_{P0}$ . Equations 5-7 show the calculations, where  $\Omega$  is the rotational speed ( $rad/s$ ) and  $A$  is the propeller disk area.

$$C_{T0} = \frac{T}{\rho A (\Omega R)^2} \quad (5)$$

$$C_{P0} = \frac{P}{\rho A (\Omega R)^3} \quad (6)$$

$$FM = \frac{(C_{T0})^{\frac{3}{2}}}{\sqrt{2} C_{P0}} \quad (7)$$

This recalculation is a unique case in regards to UAV’s, specifically if the propulsion is being used as a propeller (forward flight) or rotor (hover). As stated by Prior [20]: in the context of drones, the application of propellers has been adapted beyond their original intended use of forward flight to rather function in a manner identical to that of rotor-craft, hence the calculations should change depending on the test state.

### C. CFD Setup

With the increasing power of computational hardware, using numerical simulations to study sound fields has become a popular approach. However, the use of a direct method to obtain the aeroacoustics is out of scope in this study due to storage, time, and budget requirements. Therefore, here we employ a hybrid approach in which CFD simulations are used to resolve the flow field and provide source data on the body surface, while an acoustic analogy is used to calculate the noise propagation in the far-field based on the source data. CFD Simulations were conducted using the commercial software ANSYS Fluent (2023 R1) to solve the unsteady incompressible, Navier Stokes equations. Since flows around rotating propellers are turbulent in nature, accurate acoustic propagation strongly depends on the quality of the flow field being resolved. In this context, LES is selected for this study as it offers an efficient and reasonably affordable simulation scheme for resolving the large energy-carrying turbulent eddies and for modeling the small-scale dissipative ones. Using a sliding mesh technique, in which the propeller is placed inside a rotating domain and spun around the origin for six rotations per simulation. The remaining computational domain was static and had a cylindrical geometry. The FW-H acoustics analogy, applicable to flows with arbitrary moving boundaries such as rotating propellers, was used for calculating the noise generation and propagation, for which 16 receivers were placed on a circle around the propeller (of radius  $0.54m$ ), with a receiver every  $22.5^\circ$ . The solver settings are stated in Table 2. Figure 5 shows the domain setup for the CFD calculations, while Figure 6 shows the location of the receivers used for the estimation of the far-field acoustics. In Figure 5 the top and side surfaces were set to pressure inlet boundaries, the bottom surface set as a pressure outlet, and the solid blade surface set as a no-slip boundary. The dimensions of the domain are all scaled by the diameter of the propeller  $D$ .

**Table 2 Numerical Simulation Setup**

Numerical Settings	
Time Advancement Method	Transient-Fixed
Solver Type	Pressure Based
Velocity Formulation	Absolute
Viscous Model	Large Eddy Simulation (LES)
Subgrid-Scale Model	WMLES
Acoustics Model	FW-H
Spatial Discretisation-Pressure	Second Order
Spatial Discretisation-Momentum	Bounded Second Order Implicit
Inlet Velocity	$0ms^{-1}$
Outlet Pressure Gradient	$0Pa$

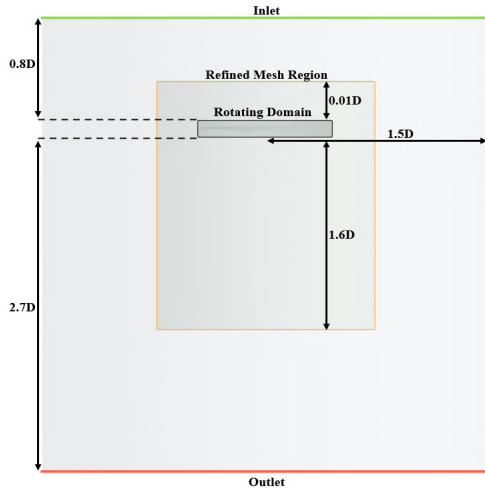


**Fig. 5 Computational Domain (Cylindrical)**

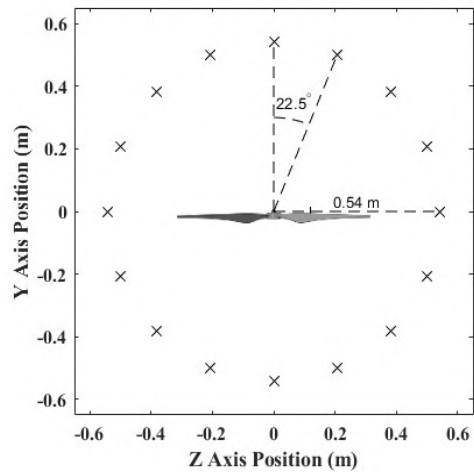


**Fig. 6 Receiver Point Locations (Propeller Enlarged for visibility)**

ANSYS Meshing was used to discretise the fluid domain using tetrahedral elements for the bulk volume and a hexahedral mesh near the blades surface to capture the boundary layer using an inflation layer approach. During the meshing process, it was discovered that the complex geometry on the looped propeller blades did not allow for an inflation layer to be grown from the surface of the propellers upwards - attempting this resulted in a minimum orthogonal quality of less than 0.01 on some cells in the inflation region, preventing the solver from running. As a solution, the inflation layer was created by growing the inflation layer downwards from the 99% boundary layer height towards the surface of the propeller. The resultant mesh can be seen in Figures 7 and 8.

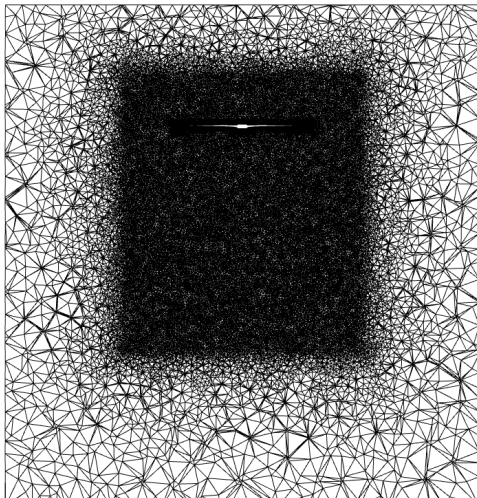


**Fig. 7 Computational Mesh**

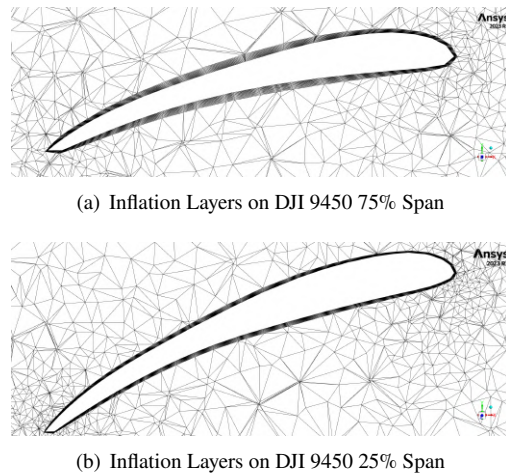


**Fig. 8 Inflation Layers**

Although this method created the inflation layer with an acceptable orthogonal quality, it did not control the  $Y^+$  to the same extent. To ensure that an acceptable value was achieved, the  $Y^+$  was plotted on the surface of all the propellers showing that the average value obtained was less than 5, as can be seen in Figure 9.

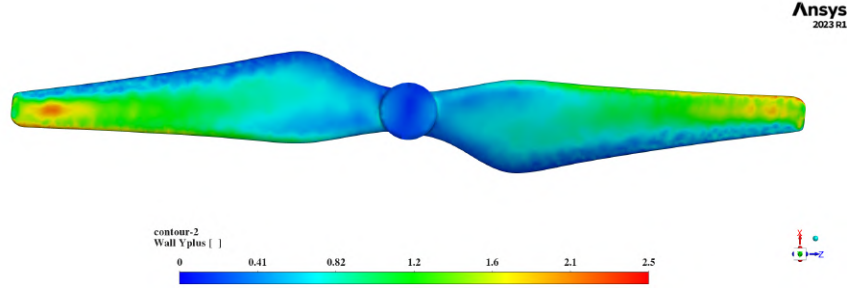


**Fig. 9**  $Y^+$  on DJI 9450 Propeller

The resulting mesh featured 7,143,181 cells and 1,277,696 nodes with the quality metrics shown in Table 3.

**Table 3** Mesh Quality Metrics

Orthogonal Quality		Skewness		Element Quality	
Min	Average	Min	Average	Min	Average
3.17E-02	0.7485312	3.15E-08	0.21406	6.41E-03	0.82917

Due to the  $Y^+$  value not being below 1 as required by LES sub-grid models such as Smagorinsky-Lilly, it was decided to use the WMLES (Wall Modelled Large Eddy Simulation) model. The WMLES model differs from standard LES in that it introduces a wall function dedicated to resolving the boundary layer flow. Equation 8 shows the implementation of WMLES in ANSYS Fluent.

$$v_t = f_D \min\{(Ky)^2, (C_{SMAG}\Delta)^2\}S \quad (8)$$

where  $v_t$  =turbulent viscosity,  $y$  = distance from the wall,  $K$  = von Karman constant,  $S$  is the strain rate and  $f_D$  is the wall dampening function. ANSYS states that with this implementation of the wall model, a  $Y^+ = 1$  is recommended, but that the model is formulated to tolerate higher values of  $Y^+$  [21],[22]. In this way the WMLES is similar to DDES but with a crucial difference, in that DDES employs a shielding function to prevent eddies from entering the boundary layer, this is not present in WMLES thus, eddies are able to cross over into the boundary layer region.

The time-step size ( $\Delta t$ ) was based on the rotational speed of the propellers. For acoustic simulations, the time step size was set so that the propeller rotated 3 degrees every time-step at 6000RPM. This allows for a frequency range up to 6000Hz to be captured for the acoustics [2]. Due to computational costs and limitations on computing facilities, all performance simulations from 3000RPM to 5000RPM were done at 5 degrees of rotation per time-step.

The CFD simulations for the DJI9450 were compared with the experimental thrust coefficient data at 3000RPM 4000RPM and 5000RPM (Table 4) to ensure that the CFD results were within an acceptable range.

**Table 4** Comparison of CFD and Experimental  $C_T$  for DJI 9450 Propeller

RPM	Experimental $C_T$	CFD $C_T$	%Difference
5000	0.0802	0.088	9.27
4000	0.08035	0.089	10.22
3000	0.077	0.086	11.04

Although there is approximately 10% average error between the two estimates, it was considered acceptable to conclude that the CFD simulations are adequate.

#### D. Experimental Setup

The experiments involved force and aeroacoustic measurements. For testing propeller thrust and efficiency performance, a Tyto Robotics Series 1520 thrust rig was placed in UWE Bristol's wind tunnel (2.54m width and 1.5m height) and paired with a T-Motor AT2317 brushless motor as pictured in Figure 10. The motor's height is positioned at 0.75m from the bottom of the wind tunnel, which coincides with the centre point of the wind tunnel. The propellers were tested in both static conditions and non-static conditions. For non-static conditions, the wind tunnel velocities are set in a range from  $2ms^{-1}$  to  $7ms^{-1}$ . Because of the size of the wind tunnel test section and the relatively small diameter of the propellers, wind tunnel corrections were not needed. The test conditions are presented in Table 5.

**Table 5 Wind Tunnel Test Conditions**

Freestream Velocity, $ms^{-1}$	Freestream Mach Number
2	0.005793
3	0.00869
4	0.011586
5	0.014482
6	0.01738
7	0.020275

It is important to note that due to the design of the thrust stand, the RPM is not set by the user, instead the rotational speed is controlled through an ESC pulse signal in  $\mu s$ , resulting in slight variations to in the RPM observed when the freestream velocity changed and when the propeller being tested changed. The results were gathered using the thrust rig's commercial software, RCBenchmark. The software was set up to run pre-made test scripts and export the Thrust, RPM and power data from the rig at a sampling rate of 20Hz. The thrust rig was also paired with a high-speed camera and a smoke generator (Figure 11) to visualise the tip vortex created by the propellers and subsequent flow interactions.

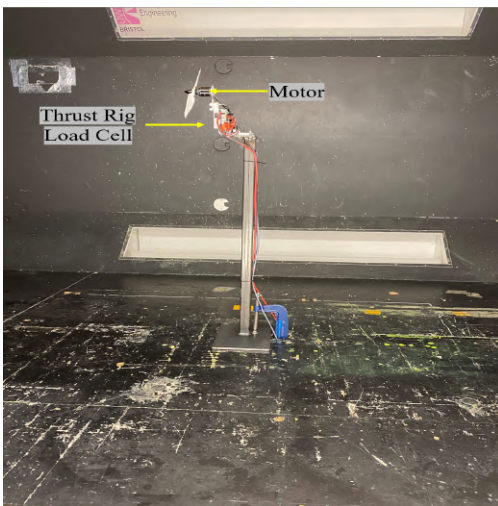


**Fig. 10 Thrust Stand in UWE, Bristol Wind Tunnel**

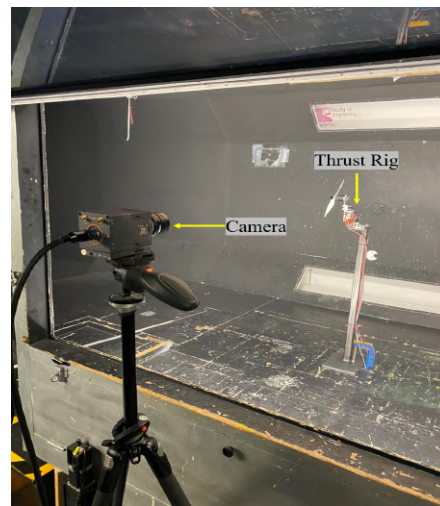


**Fig. 11 High-Speed Camera Setup**

For acoustics testing, the thrust rig was placed in UWE Bristol's anechoic chamber. The far-field noise generation was measured using a DPA 4006C condenser probe microphone, which was set up at a distance of 0.54m directly behind the propeller. The propeller was then rotated at 4000RPM to measure the generated noise levels. The software (REW Room EQ Wizard) used to estimate the noise was set to capture a frequency range between 50Hz and 6000Hz to match a similar data range to the CFD data. The acoustic setup can be seen in Figure 12. Calibration of the microphone was conducted using an external sound level meter with an accuracy of  $\pm 2$  dB. It is worth noting that the testing conditions

for the propellers were set such that no flow-induced vibration noise was created, meaning that only aerodynamic noise was considered.



**Fig. 12 Acoustic Testing Setup in UWE Bristol’s Anechoic Chamber**

### III. Results

The numerical and experimental investigations, as outlined in the methodology, yielded a comprehensive dataset, which is presented and discussed herein. The results have been split into two distinct sections for the CFD results and the experimental results.

#### A. CFD Results

##### 1. Acoustics Results

The acoustic analysis for the numerical results was done first by analysing the overall sound pressure levels (OSPL), experienced at each receiver location. The OSPL represents a single value to describe the intensity of the sound wave across the entire captured frequency range. In this case, it was used to gain an understanding of how the sound propagates in a  $360^\circ$  arc around the propeller. The OSPL results are presented in Figures 13 and 14 for the DJI and APC propeller sets, respectively.

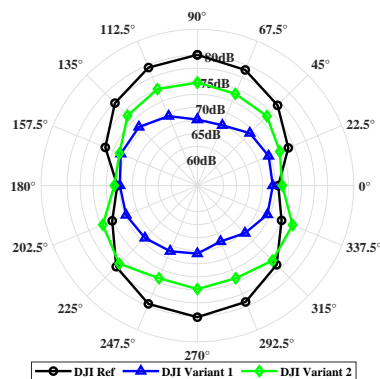


**Fig. 13 DJI Propeller Set OSPL**

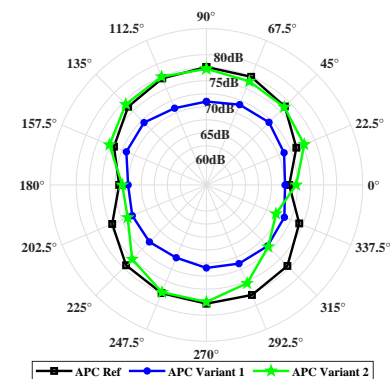


**Fig. 14 APC Propeller Set OSPL**

When looking at the results, the noise reduction is clear for Variant 1 in both propeller sets, with the largest reduction in noise generation occurring in the vertical axis above and below the propellers ( $270^\circ$  and  $90^\circ$ ). Upon close investigation of the DJI Variant 2’s results, it can be seen that it does not offer as large of a noise reduction benefit and is

actually potentially detrimental towards the sides of the propeller. A similar effect is seen with the APC Variant 2, with very little noise benefits and some results towards the sides of the propeller being slightly louder.

Further analysis of the acoustics data was performed using the data captured from receiver 270°. The raw SPL against the frequency data is plotted in Figures 15-16.

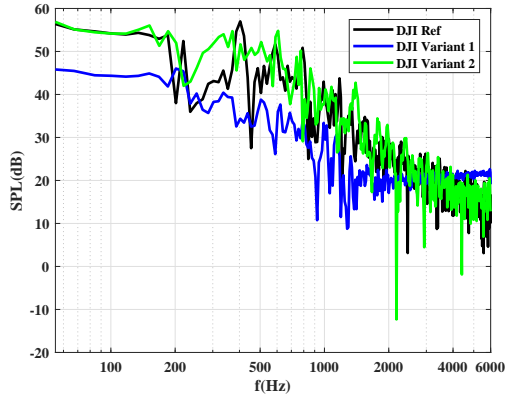


**Fig. 15 DJI Propeller Set SPL vs Frequency**

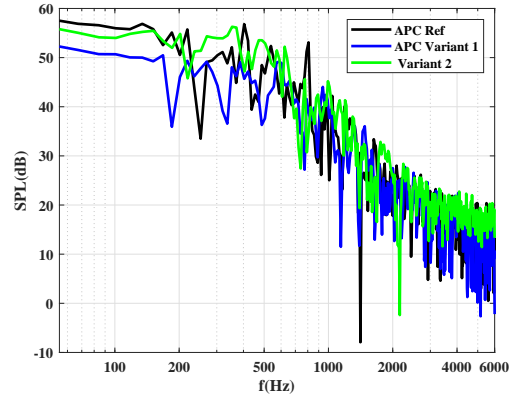


**Fig. 16 APC Propeller Set SPL vs Frequency**

Looking at Figures 15 and 16 shows Variant 1 being noticeably quieter for both propeller sets, with the largest reductions occurring in the low-frequency range. For the DJI set, noise reductions for Variant 1 occur over frequencies of up to just over 2000 Hz, whereas for the APC set noise reduction benefits cease beyond 600 Hz. Both sets of Variant 2 propeller results show similar SPL trends across the full frequency range. To better understand how the noise generated by the propellers would be interpreted by the human ear (Perceived Noise Levels), an A-weighting was applied to the data as can be seen in Figures 17 and 18.

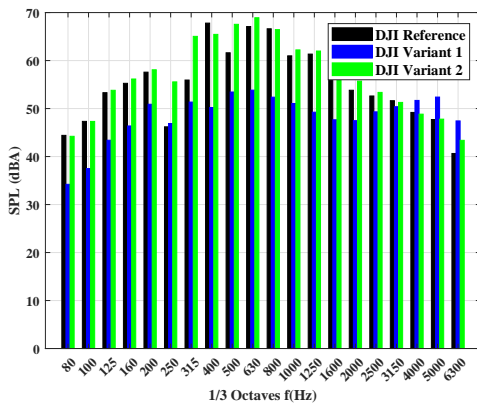


**Fig. 17 DJI Set A Weighted SPL vs Frequency**

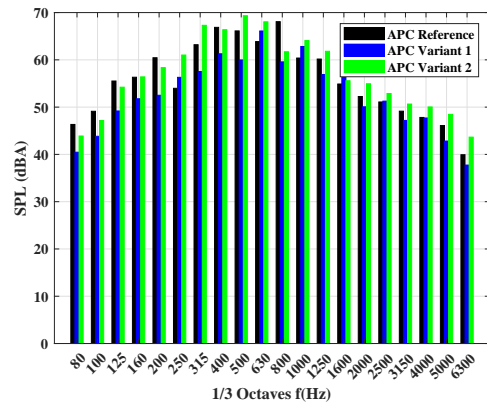


**Fig. 18 APC Set A Weighted SPL vs Frequency**

In both propeller data sets it is evident that Variant 1 offers larger noise reduction benefits across the frequency range. The largest reduction in SPL for Variant 1 in the DJI set occurs at the 400 Hz frequency 1/3 octave band. Similarly, for the APC set, Variant 1 achieves its greatest noise reduction at the 800 Hz frequency 1/3 octave band.

## 2. Flow Behaviour

To better understand the differences in noise generation from the propellers, the flow behaviour was studied in the CFD results using contours of the small pressure fluctuations on the surface of the propellers, and through visualisations of the tip vortex generation and propagation. The acoustic surface pressure fluctuation visualisations provide insightful

data on the different noise generation characteristics of the propellers as shown in Figures 19-21.

The reference propeller (Figure 19) shows a clear contour of acoustic pressure, with the highest intensities at the blade tip, demonstrating the fluctuations created by interactions with the tip vortex patterns. In comparison, Variant 1 (Figure 20) displays a more uniform distribution of acoustic pressure across the blade, with less pronounced intensities towards the tip. This suggests a reduction in interactions between the propeller blade and the tip vortices.

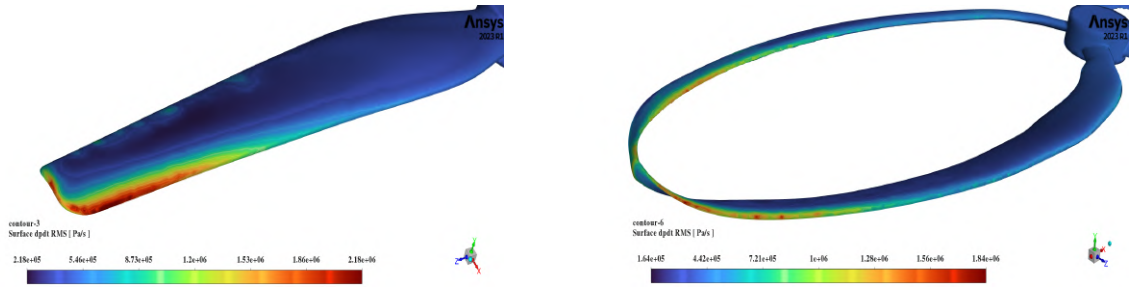


**Fig. 19 DJI 9450 Surface Pressure Fluctuations**      **Fig. 20 DJI Variant 1 Surface Pressure Fluctuations**

Viewing the results from Variant 2 (Figure 21), a more even distribution of the pressure fluctuations is also noted, but the maximum regions consist of a higher magnitude when compared with Variant 1. This suggests that although the design succeeded at gaining a better distribution of the sound generating pressure fluctuations, it still does not reduce the intensity of the sound, hence reinforcing the findings of the acoustics analysis.

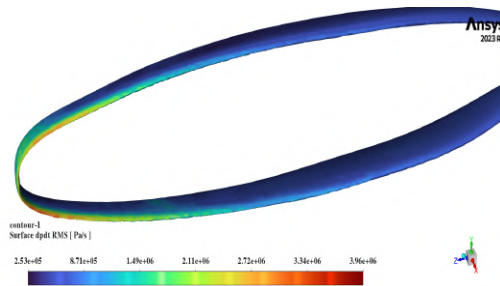


**Fig. 21 DJI Variant 2 Surface Pressure Fluctuations**

To further understand the impact of the vortex formations at the tip, velocity magnitude streamlines were plotted in Figures 22-24 for the DJI set.

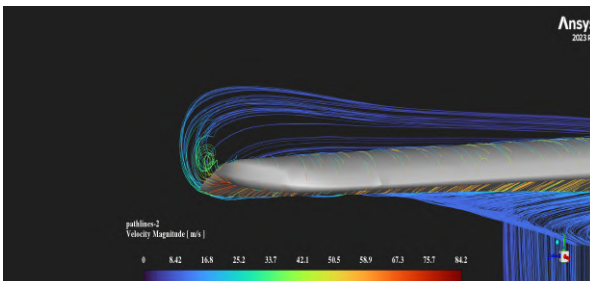


**Fig. 22 DJI 9450 Single Observed Tip Vortex**

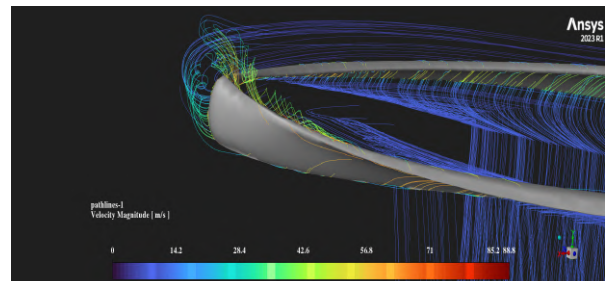


**Fig. 23 DJI Variant 1 Dual Contra-Rotating Tip Vortex**

The standard DJI 9450 propeller (Figure 22) displays a well-defined clockwise tip vortex, indicative of conventional propeller operation. This is in contrast to Variant 1 (Figure 23) which reveals what seems to be a dual contra-rotating vortex pattern. This suggests that Variant 1 disrupts the strength of the vortex by splitting it into two weaker vortices

that work against each other when they merge behind the propeller blade, thereby leading to less pronounced pressure fluctuations. In the case of Variant 2, a completely different flow interaction is observed, as seen in Figure 24.

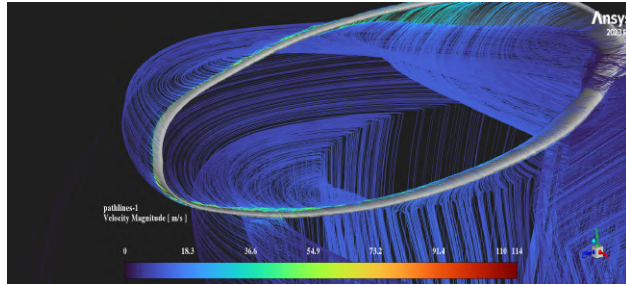


**Fig. 24 DJI Variant 2 No Vortex Formation**

From Figure 24 the design appears to have generated less distinct vortices - instead it creates a larger wake flowfield, which is of particular note, as it shows the interaction of the lower blade with the wake of the opposite blade. This may be the cause of the large tip vibrations that were observed in experimental testing at high RPMs (not reported). It also suggests an increase in blade wake interactions, in such a way that even though there has been a large reduction in blade vortex interaction, it has not translated to an overall reduction in noise emitted from the propeller.

## B. Experimental Results

### 1. Static Performance Results

Figures 25 and 26 show the thrust coefficient performance of the DJI and APC propeller sets, respectively, versus RPM. When comparing the looped variants to their respective reference designs, it can be seen in both cases that the looped configurations produce less thrust at the same RPM. It should be noted that some of the performance reduction may be attributed to flexing in the propellers, as the looped variants were found to experience notable tip oscillations which may have had a detrimental effect on the performance.

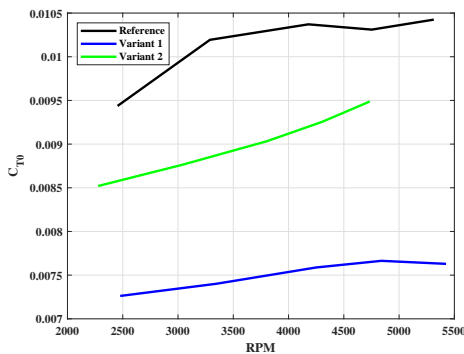


**Fig. 25 DJI Set Thrust Coefficients**

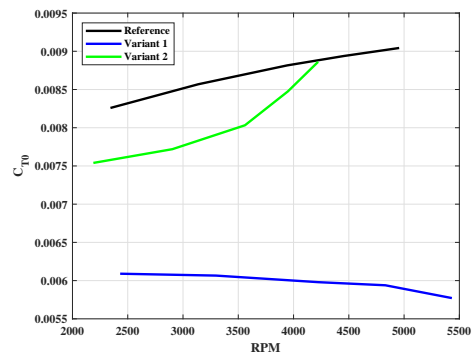


**Fig. 26 APC Set Thrust Coefficients**

In comparison with the reference configuration, Variant 1 of the DJI set produced an average reduction (across the RPM range) of 25.9% in  $C_T$ , while a 11.2% average  $C_T$  reduction was observed across Variant 2. A similar trend is seen for the APC propeller set which experiences a 29% average reduction in  $C_T$  for Variant 1 and a 9.4% reduction for Variant 2.

It is also observed that with the same ESC pulse lengths, in both sets Variant 2 was not able to achieve as high of an RPM, implying that Variant 2 has a much higher resistance to motion when compared with the respective reference propellers. This observation is further reinforced when looking at the power coefficient plots in Figures 27-28.

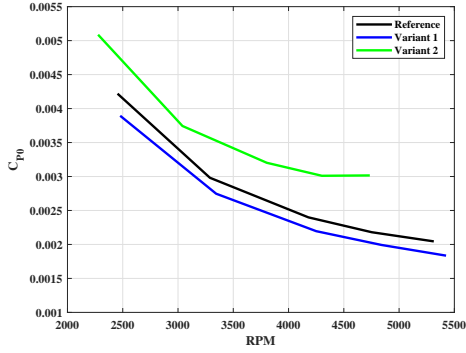


**Fig. 27 DJI Set Power Coefficients**

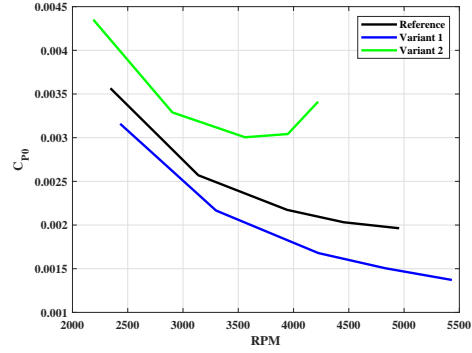


**Fig. 28 APC Set Power Coefficients**

As can be seen in Figures 27 and 28, for both the DJI and APC sets, Variant 2 has much larger  $C_P$  values when compared to the reference propellers. This demonstrates that Variant 2 has higher power requirements and hence leading to a reduction in operational efficiency. In contrast, Variant 1 experiences a lower  $C_P$  requirement than the reference propeller, though it also consistently has a lower thrust output at all RPMs (as already seen in Figures 25 and 26).

The overall reduction on efficiency of Variant 1 and 2 is best demonstrated when plotting their Figure of Merit in Figures 29-30. When looking at the obtained FM values, it can be seen that in both sets, Variant 1 and Variant 2 produce very similar FM values despite differing behaviours of their respective  $C_T$  and  $C_P$  data. Whilst for Variant 1 the lower power requirements are offset by lower thrust outputs, for Variant 2 the higher thrust values are offset by higher power requirements.

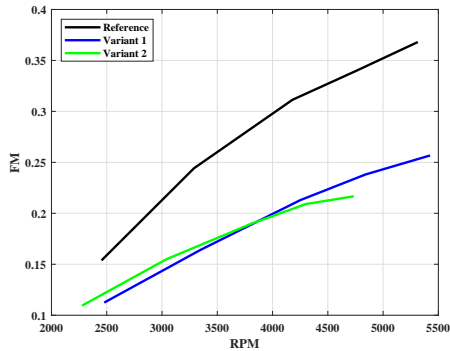


**Fig. 29 DJI Set Figure of Merit**

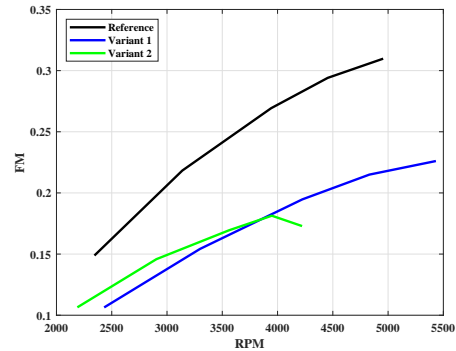


**Fig. 30 APC Set Figure of Merit**

## 2. Non-Static Performance Results

The non-static results were obtained with the wind tunnel at set increments of freestream velocity ( $V$ ) from  $2m s^{-1}$  to  $7m s^{-1}$ . A notable behavioral change in Variant 2 of the APC set, when compared to Variant 2 of the DJI set, warrants attention. During this phase, Variant 2 of the APC set exhibited noticeably large tip oscillations—significantly more so than in static tests, these increased tip oscillations prevented APC Variant 2 from being able to reach more than 3500RPM. This anomaly is suspected to stem from manufacturing defects in APC Variant 2, leading to damage, which further leads to a substantial performance degradation under dynamic testing conditions. This theory could not be validated in a materials lab though due to time constraints and project scope limitations, but the results of APC Variant 2 were included in the non-static performance results for continuity purposes.

Analysing the thrust coefficient plots in Figures 31-32, it can be seen that the relationship between Variant 1 and 2 in both propeller sets remains similar to that found during the static testing - with Variant 1 producing on average, a 30%

loss in  $C_T$ . It should be noted in the Case of DJI Variant 1, the propeller did not suffer a loss of  $C_T$  to the same extent as the DJI reference and Variant 1 propellers, suggesting the propeller has a greater range of viable operating speeds.

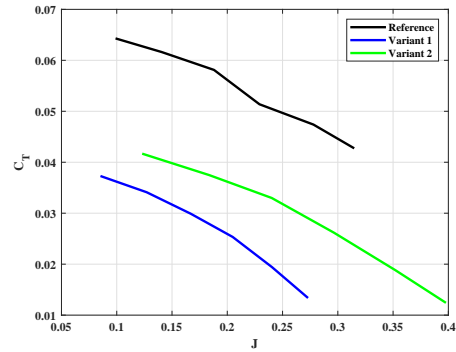
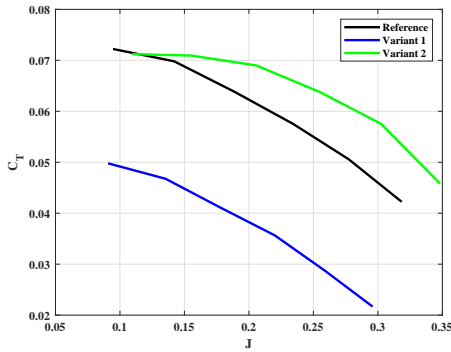


**Fig. 31 DJI Set Thrust Coefficient vs Advance Ratio Fig. 32 APC Set Thrust Coefficient vs Advance Ratio**

The  $C_P$  and efficiency results shown in Figures 33-36 again exhibit similar trends as those observed in the static results, where the increased  $C_P$  required for Variant 2 leads to Variant 1 in both sets having a similar efficiency ( $\eta$ ). It is of note that in both sets the efficiency curve for Variant 1 drops off at a much earlier advance ratio (J) when compared to the reference propellers and Variant 2, this suggests a much lower range of suitable operating speeds are available to Variant 1.

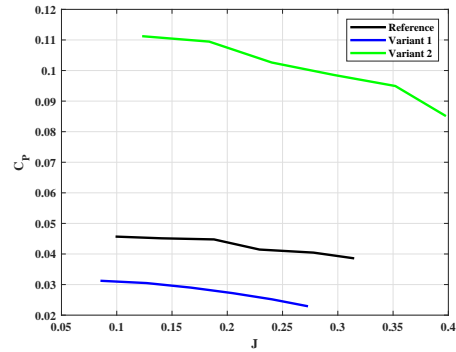
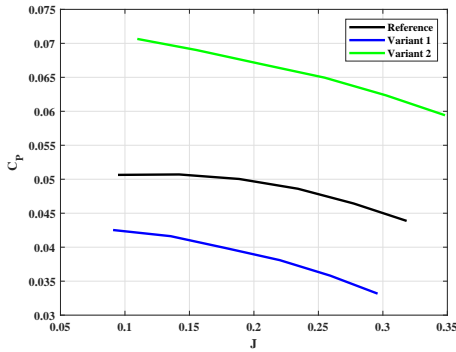


**Fig. 33 DJI Set Power Coefficient vs Advance Ratio Fig. 34 APC Set Power Coefficient vs Advance Ratio**

For DJI set Variant 2, its efficiency is lower than that of Variant 1 for advance ratios less than about 0.18, then becomes much higher than Variant 1 (peak value at  $J=0.3$ ). However, for APC set Variant 2, its efficiency is significantly lower than that of Variant 1 across the full range of advance ratio.

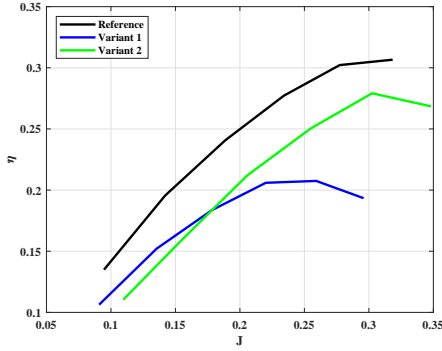


**Fig. 35 DJI Set Efficiency vs Advance Ratio**

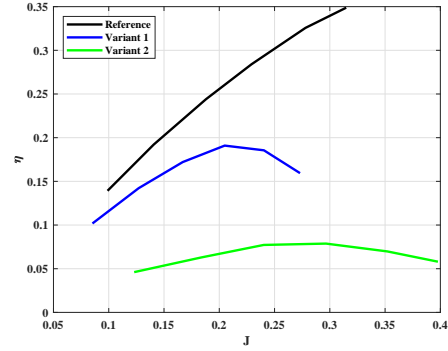


**Fig. 36 APC Set Efficiency vs Advance Ratio**

### 3. Acoustics Results

Acoustic testing was conducted at a constant 4000RPM within the anechoic chamber at UWE Bristol for hovering conditions only. Given that the motor’s acoustic signature is included with that of the propeller, a comparative analysis was conducted to find the frequencies at which the motor noise was captured so they can be removed from the aerodynamic noise. The results of this analysis are plotted in Figures 37-38.

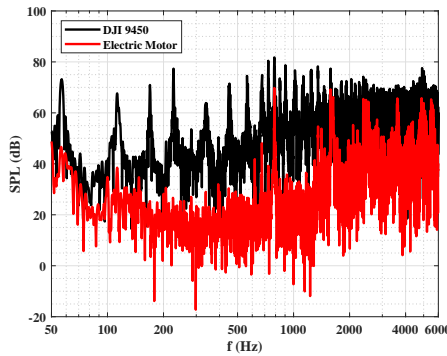


**Fig. 37 DJI 9450 SPL vs Frequencies with Motor**

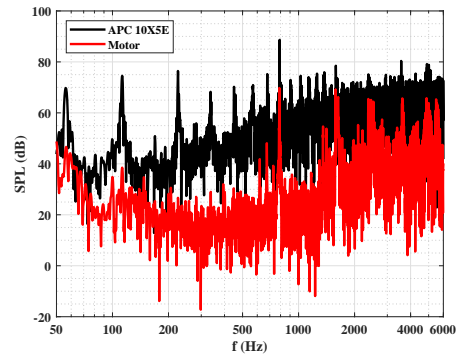


**Fig. 38 APC 10X5E SPL vs Frequencies with Motor**

The results show that the electric motor’s noise experiences a large increase at a frequency of 1300Hz, and from there onwards becomes the dominant noise source heading into the high frequencies. Hence to appropriately analyse the propeller aerodynamic noise, the results were limited from 50Hz to 1250Hz as shown in Figures 39-41. It is to be noted that no noise test could be completed in APC Variant 2 as attempting to reach a rotational speed close to 4000RPM with the damage to the propeller resulted in excessive vibrations in the thrust rig, leading to inaccurate results which varied wildly when the test was repeated, hence only Variant 2 of the DJI set is shown in the results.

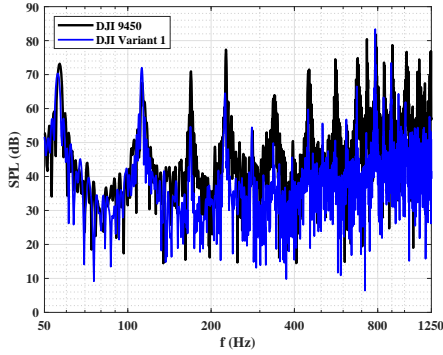


**Fig. 39** DJI 9450 and DJI Variant 1 Acoustics

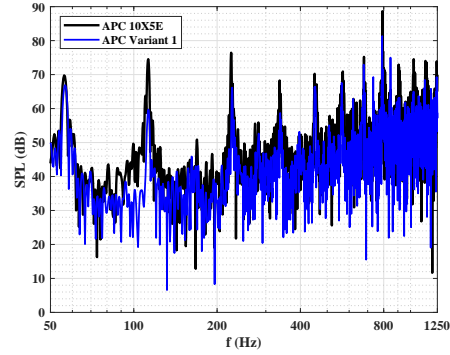


**Fig. 40** APC 10X5E and APC Variant 1 Acoustics

In both data sets it is evident that Variant 1 experiences reductions in SPL across the entire frequency range. For the DJI Variant 1 propeller the greatest reductions in SPL occur between 400Hz and 800Hz (Figure 39). For the APC propeller, the largest reductions occur between 60Hz and 300Hz (Figure 40). The blade passing frequency can also be seen in the data with large spikes occurring at 133Hz. Tonal noise reductions can be seen in both propeller sets across the entire captured frequency range in the large intermittent spikes. The noise reductions in these regions appear to be much larger compared to the noise reductions between the tonal spikes, suggesting that although Variant 1 reduces the noise generated in both the broadband and tonal noise, the reductions are much more impactful for tonal noise.

Variant 2 for the DJI set's results can be seen in Figure 41. The results once again match what was expected from the numerical data, with Variant 2 being slightly louder across the tested frequency range, with a large spike in SPL at 230 Hz reaching up to 90dB.

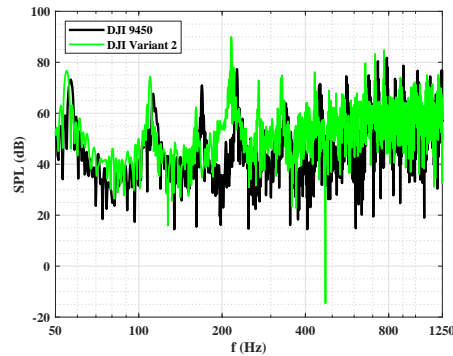


**Fig. 41** DJI 9450 and DJI Variant 2 Acoustics

#### 4. Flow Behaviour

To visualise the variations in flow behavior, each propeller was set to rotate at the RPM corresponding to a thrust output of 1 Newton ( $\sim 4000RPM$ ). Subsequently, slow-motion footage was captured with smoke introduced at the propeller tips to visualize the formation of tip vortices. A ruler was placed in the background of the footage and overlaid on the images to measure the distance before the vortex begins to dissipate into the flow. This was only done with the DJI set due to time limitations. The results of the process can be seen in Figures 42-43.



**Fig. 42 DJI 9450 Tip Vortex**

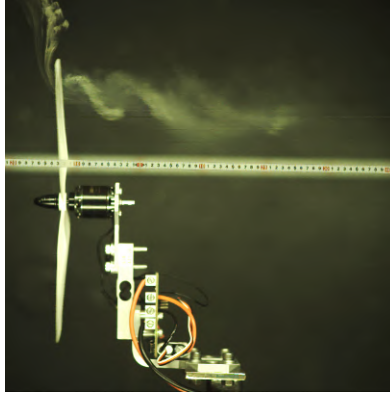


**Fig. 43 DJI Variant 1 Tip Vortex**

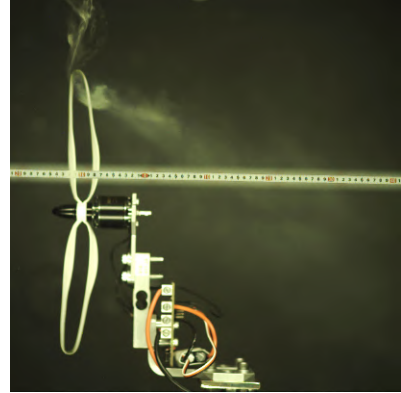


**Fig. 44 DJI Variant 2 Tip Vortex**

The reference DJI 9450 propeller demonstrated a well-defined vortex that appears to maintain its structure further from the blade tip before dissipating into the flow. This clarity and coherence in the vortex suggest that the flow remains relatively ordered as it leaves the propeller tip. In contrast, the vortices from DJI Variants 1 and 2 show notable differences. Variant 1 produces a vortex that begins to diffuse sooner and more broadly compared to the reference model. This implies that there may be a reduction in the overall strength of the tip vortex, hence leading to a reduction in the noise generated by the blade vortex interactions. In Variant 2, the tip vortex shows a considerable disruption in the smoke pattern, this was confirmed in viewing the video as the lower blade portion was cutting through the vortex as it begins to form. This may possibly be the reason behind the increased power requirements to achieve the same RPM's as the reference propeller and Variant 1, due to increased aerodynamic resistance.

The main conclusion from these simple flow visualisations is that the looped propeller variants can disrupt and partially suppress the formation of the tip vortices compared with the reference configuration. Consequently, the looped variants have a reduced level of blade tip-vortex and tip-vortex wake interactions, all of which lead to reductions in the measured far-field noise. However, this may only be achieved as long as the looped blades do not undergo structural vibrations (tip oscillations in this case) which would increase noise.

#### **IV. Conclusions and Further Research**

This study's investigation into the aerodynamic and aeroacoustic characteristics of looped propeller blades presents a significant departure from traditional UAV propeller configurations, providing substantial evidence to support their potential in mitigating noise emissions. The results indicate that Variant 1 achieves a considerable reduction in sound pressure levels, offering a viable option for applications that require reduced noise footprints. However, this benefit is offset by a decrease in thrust coefficient and propeller efficiency, underscoring the intricate balance between noise suppression and aerodynamic performance. These findings are further reinforced by the work of Shima et, al. [15] in which similar losses in  $C_T$  and efficiency were found. The reductions in aerodynamic noise are also reinforced by MIT's findings [8], who experienced similar noise reductions for the in-plane looped propeller (Variant 1)

The flow behavior analyses, with their focus on the propeller tip vortices, highlighted a mechanism contributing to the noise reduction observed in Variant 1. In contrast, Variant 2, records an increase in SPL due to more pronounced blade wake interactions and possibly due to observed tip oscillations, particularly in the lower blade region, leading to Variant 2 in the APC set being susceptible to structural damage. These findings have provided insight into the interplay between design modifications and their aerodynamic and aeroacoustic outcomes.

Acknowledging the material limitations encountered, this research underscores the need for an exhaustive investigation into alternative materials and fabrication methods. The pursuit of materials with the desired stiffness and durability is essential for the practical application of looped propeller designs and the realization of their full potential. As a further recommendation, the following research trajectories are proposed:

- The contrasting performance profiles of Variant 1 and Variant 2 suggest the exploration of a hybrid design, similar to the Sharrow Marine Propeller [9], which may combine the desirable attributes of both variants.
- The integration of bio-mimicry techniques, such as leading-edge tubercles and trailing-edge serrations, with Variant 1, could offer a possibility for increasing the propeller's efficiency without sacrificing its noise reduction capabilities.
- Extending the scope to include propellers with more than two blades could unveil new performance and noise reduction opportunities, allowing for a wider range of use cases e.g. the standard quadcopter designs.
- Testing the designs with various materials and manufacturing methods, to further understand the structural limitations and manufacturing implications of looped propeller designs.
- A parametric study should be conducted, to optimise the shape of the looped blades, in attempt to minimise performance loss.

Overall, this study serves as exploratory research into understanding the effects of looped blade designs. The results achieved justify that these propellers are deserving of additional research, as a potential candidate and solution to quieter propeller designs not only for drones but for VTOLs and may potentially be scalable to larger designs.

### **Acknowledgements**

The authors would like to express their thanks to technicians Peter Robson and to Lucy Corfield at the University of the West of England for their respective help in the experimental setup and 3D printing, and to Saif Majid for his support on CFD setup. The authors also acknowledge UWE's support by providing access to the Rescale facility which enabled the LES computations.

## References

- [1] Stokkermans, T. C. A., and Veldhuis, L. L. M., “Propeller Performance at Large Angle of Attack Applicable to Compound Helicopters,” *AIAA Journal*, Vol. 59, No. 6, 2021, pp. 2183–2199. <https://doi.org/10.2514/1.J059509>.
- [2] Wilkins, R., and Bouferrouk, A., “Numerical framework for aerodynamic and aeroacoustics of bio-inspired UAV blades,” 2023. <https://doi.org/10.13009/EUCASS2023-948>.
- [3] Romani, G., and Casalino, D., “Rotorcraft blade-vortex interaction noise prediction using the Lattice-Boltzmann method,” *Aerospace Science and Technology*, Vol. 88, 2019, pp. 147–157. <https://doi.org/https://doi.org/10.1016/j.ast.2019.03.029>, URL <https://www.sciencedirect.com/science/article/pii/S1270963818321011>.
- [4] Wu, J., Stalnov, O., Chen, W., Yang, Z., and Huang, X., “Transient analysis of blade-vortex interaction noise,” *Aerospace Science and Technology*, Vol. 120, 2022. <https://doi.org/10.1016/j.ast.2021.107294>.
- [5] ANSYS, *ANSYS Fluent Theory Guide*, 2021, Chap. 11: Aerodynamically Generated Noise, pp. 405–420. URL [https://dl.cfdexperts.net/cfd\\_resources/Ansys\\_Documentation/Fluent/Ansys\\_Fluent\\_Theory\\_Guide.pdf](https://dl.cfdexperts.net/cfd_resources/Ansys_Documentation/Fluent/Ansys_Fluent_Theory_Guide.pdf).
- [6] Marte, J. E., and Kurtz, D. W., “A Review of Aerodynamic Noise From Propellers, Rotors, and Lift Fans,” Tech. rep., NASA, 1970. URL <https://ntrs.nasa.gov/api/citations/19700005920/downloads/19700005920.pdf>.
- [7] Hanson, L. P., Baskaran, K., Pullin, S. F., Zhou, B. Y., Zang, B., and Azarpeyvand, M., *Aeroacoustic and Aerodynamic Characteristics of Propeller Tip Geometries*, 2022. <https://doi.org/10.2514/6.2022-3075>.
- [8] “Toroidal Propeller,” Technology Highlight 41, MIT Lincoln Laboratory, Feb 2023. URL [https://www.ll.mit.edu/sites/default/files/other/doc/2023-02/TVO\\_Technology\\_Highlight\\_41\\_Toroidal\\_Propeller.pdf](https://www.ll.mit.edu/sites/default/files/other/doc/2023-02/TVO_Technology_Highlight_41_Toroidal_Propeller.pdf), accessed: September 12, 2023.
- [9] BoatTEST.com, “Sharrow Propeller™ Evaluation,” Available: <https://boattest.com/Sharrow-Propeller>, Feb 2023. Accessed: September 12, 2023.
- [10] Van Treuren, K., Wisniewski, C., and Cinnamon, E., “Near and Far Field Noise Decay From a Quadcopter Propeller With and Without a Leading Edge Notch,” 2018, p. V001T01A021. <https://doi.org/10.1115/GT2018-75973>, URL <https://doi.org/10.1115/GT2018-75973>.
- [11] Jordan, W. A., Narsipur, S., and Deters, R., *Aerodynamic and Aeroacoustic Performance of Small UAV Propellers in Static Conditions*, 2020. <https://doi.org/10.2514/6.2020-2595>.
- [12] Harbison, D., “Phantom 3 Prop,” <https://grabcad.com/library/phantom-3-prop-1>, 2019. Accessed: February 15, 2024.
- [13] Propellers, A., “Downloads - APC Propellers,” <https://www.apcprop.com/technical-information/file-downloads/>, 2024. Accessed: February 15, 2024.
- [14] Materialise, “PA-GF for Laser Sintering,” <https://www.materialise.com/en/industrial/3d-printing-materials/pa12-gf>, 2024. Accessed: October, 2023.
- [15] Shima, E., Tsutsumi, S., and Fujimoto, K., “Preliminary Study on Innovative Loop Propellers for Quiet eVTOL,” 2019. URL [https://www.researchgate.net/publication/368189976\\_Preliminary\\_Study\\_on\\_Innovative\\_Loop\\_Propellers\\_for\\_Quiet\\_eVTOL](https://www.researchgate.net/publication/368189976_Preliminary_Study_on_Innovative_Loop_Propellers_for_Quiet_eVTOL).
- [16] Singh, M., Aloor, J. J., Singh, A., and Saha, S., “Box Wing: Aerodynamic Experimental Study for Applications in MAVs,” *National Conference on Wind Tunnel Testing NCWT-06*, 2020. <https://doi.org/10.31219/osf.io/3r79q>.
- [17] Traub, L., “Experimental Investigation of Annular Wing Aerodynamics,” *Journal of Aircraft*, 2009. <https://doi.org/10.2514/1.39822>.
- [18] Brandt, J., and Selig, M., *Propeller Performance Data at Low Reynolds Numbers*, 2011. <https://doi.org/10.2514/6.2011-1255>.
- [19] Dantsker, O., Caccamo, M., Deters, R. W., and Selig, M. S., *Performance Testing of Aero-Naut CAM Folding Propellers*, 2020. <https://doi.org/10.2514/6.2020-2762>.
- [20] Prior, S. D., *Optimizing Small Multi-Rotor Unmanned Aircraft*, CRC Press/Balkema, 2019, Chap. 5, pp. 43–44.
- [21] ANSYS, *Best Practice: Scale-Resolving Simulations in Ansys CFD*, 2015. URL <https://www.ansys.com/content/dam/product/fluids/cfd/tb-best-practices-scale-resolving-models.pdf>.
- [22] Zhang, Y., Xiao, Y., Liu, R., and Chen, H., “Aeroacoustic prediction based on large-eddy simulation and the Ffowcs Williams–Hawkings equation,” *Advances in Aerodynamics*, 2020. <https://doi.org/10.1186/s42774-022-00112-2>.